In this project, we explore data from direct numerical simulation (DNS) of two types of turbulent flow: homogeneous isotropic turbulence (HIT), and homogeneous shear turbulence (HST). Both are oft-studied flows, which exhibit many of the complexities of real-world turbulence, but are simple enough to analyze statistically. Both data sets have spatial and grid dimensions of

$$[L_x, L_y, L_z]/L = [2\pi, \pi, 2\pi] \qquad \text{(spatial dimensions)}$$
$$[N_x, N_y, N_z] = [256, 129, 256] \qquad \text{(grid dimensions)}.$$

The data is non-dimensionalized by the length scale L and the root mean square velocity u_{rms}. We will treat the data "as-is" using this scaling. Both data sets are incompressible and have the same kinematic viscosity ν everywhere. The three Cartesian coordinates $\{x, y, z\}$ have corresponding data indices $\{i, j, k\}$ and velocity components $\{u, v, w\}$. We will see that there are no significant velocity gradients in the HIT data, but that the HST data has a linear variation in mean velocity $\overline{u}$ as a function of y.

All processing is carried out in MATLAB, and a full code listing is included in a compressed directory associated with this document.

Part 1   Comparison of Velocity Fields and Statistics in HIT and HST

Problem 1.1

The maximum and minimum values of the component velocity fields in the full three dimensional volumes, for both HIT and HST are presented in Table 1.

	Max			Min		
	u	v	w	u	v	w
HIT	0.8577	0.5417	0.7064	-0.7591	-0.6006	-0.7692
HST	5.8624	3.0338	3.1315	-5.1387	-3.3306	-2.9639

Table 1: Global maximum and minimum velocities for HIT and HST.

The velocity extrema of the shear (HST) case are all roughly an order of magnitude larger than those of the isotropic (HIT) case. Within each case, maximum and minimum values of a given velocity component are of comparable magnitude. Furthermore, the non-isotropic nature of the shear (HST) case can be seen in the higher magnitude of the u-extrema. This is in contrast to the velocity magnitudes of the isotropic (HIT) case, which are all roughly equal and display no preferential direction, at least within an assumed degree of variability due to unsteadiness.

Problem 1.2

Two isosurfaces of the HIT and HST u-velocity data are presented in Figure 1, using isosurface values of $u = \frac{1}{2}\{u_{\max}, u_{\min}\}$.

Both isosurfaces in the HIT data appear to be fairly mixed and randomly located, but the volumes they enclose seem to have a mean alignment in the j-direction. This could very well be transient behavior howerver, since we are looking at a snapshot in time of an isotropic simulation. The HST isosurfaces, on the other hand, are preferentially located near the walls at $y = \{0, \pi\}$. They are
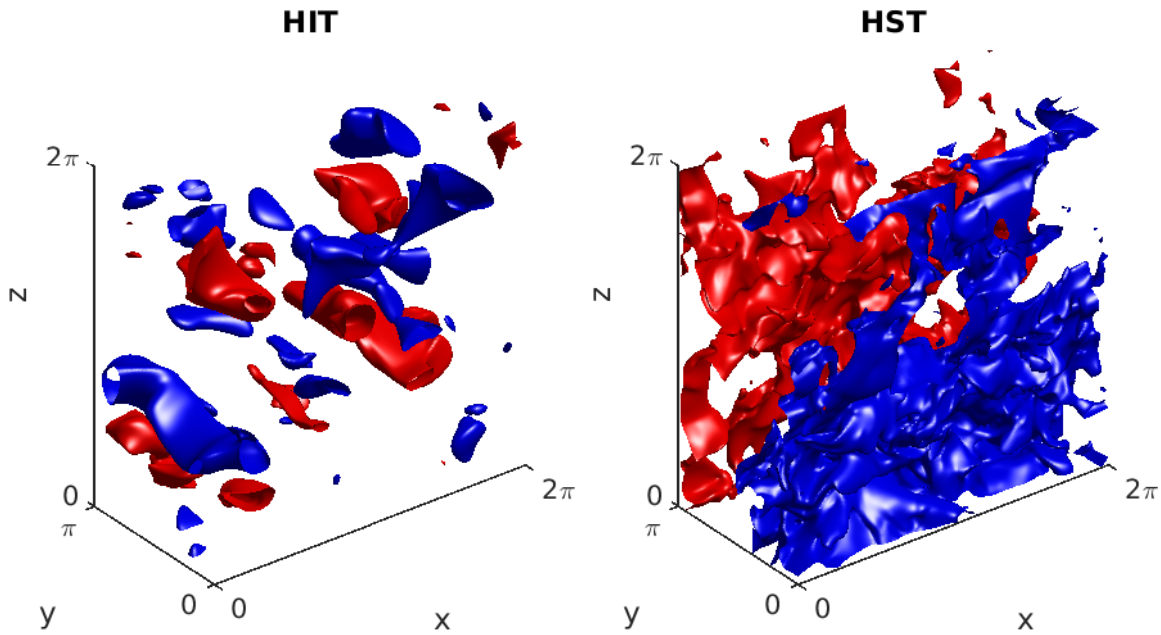
Figure 1: Isosurfaces of u-velocity at half-max in red (■) and half-min in blue (■) for HIT and HST.

also less prone to enclosing substantial volumes as in the HIT case, instead appearing as more of a sheet separating the walls from the core flow. Both HIT and HST isosurfaces have some degree of unpredictability and roughness that can be attributed to the 'random' nature of turbulence.

Problem 1.3

Figure 2 shows velocity fields u, v, and w in all three slice planes located at $k = \{1, 128, 256\}$ for both the isotropic (HIT) and shear (HST) cases.

    The isotropic (HIT) case has a much lower mean velocity and perhaps a larger viscous length scale, as velocity gradients are much smaller in magnitude compared to the shear (HST) case. This particular view of the HIT data, like the isosurface plots, shows a preferential axial direction of turbulent structures in the j-direction. As discussed previously, these structures are likely transient.

    Flow in the shear (HST) case is driven by opposing motion of the $y = 0$ and $y = \pi$ bounding planes in the i-direction, and this manifests as a large velocity gradient of u in all xy-slice planes. The velocities v and w are qualitatively similar, in that their distributions of velocities are similar. The only difference is that the structures in the w-field appear more elongated in the i-direction than those in the v-field at this instance in time.

    Within each case, the velocity components at slice planes $k = 1$ and $k = 256$ are identical. This implies use of periodic boundary conditions, at least on the z-normal domain boundaries. Periodic boundaries are likely used on all bounding planes for HIT, and on the z- and x-normal bounding planes for HST.

Problem 1.4

From the previous problems, we conclude that the homogeneous spatial directions for each case are: HIT (i, j, and k), and HST (j and k). We expect the flow statistics to be invariant along these directions.
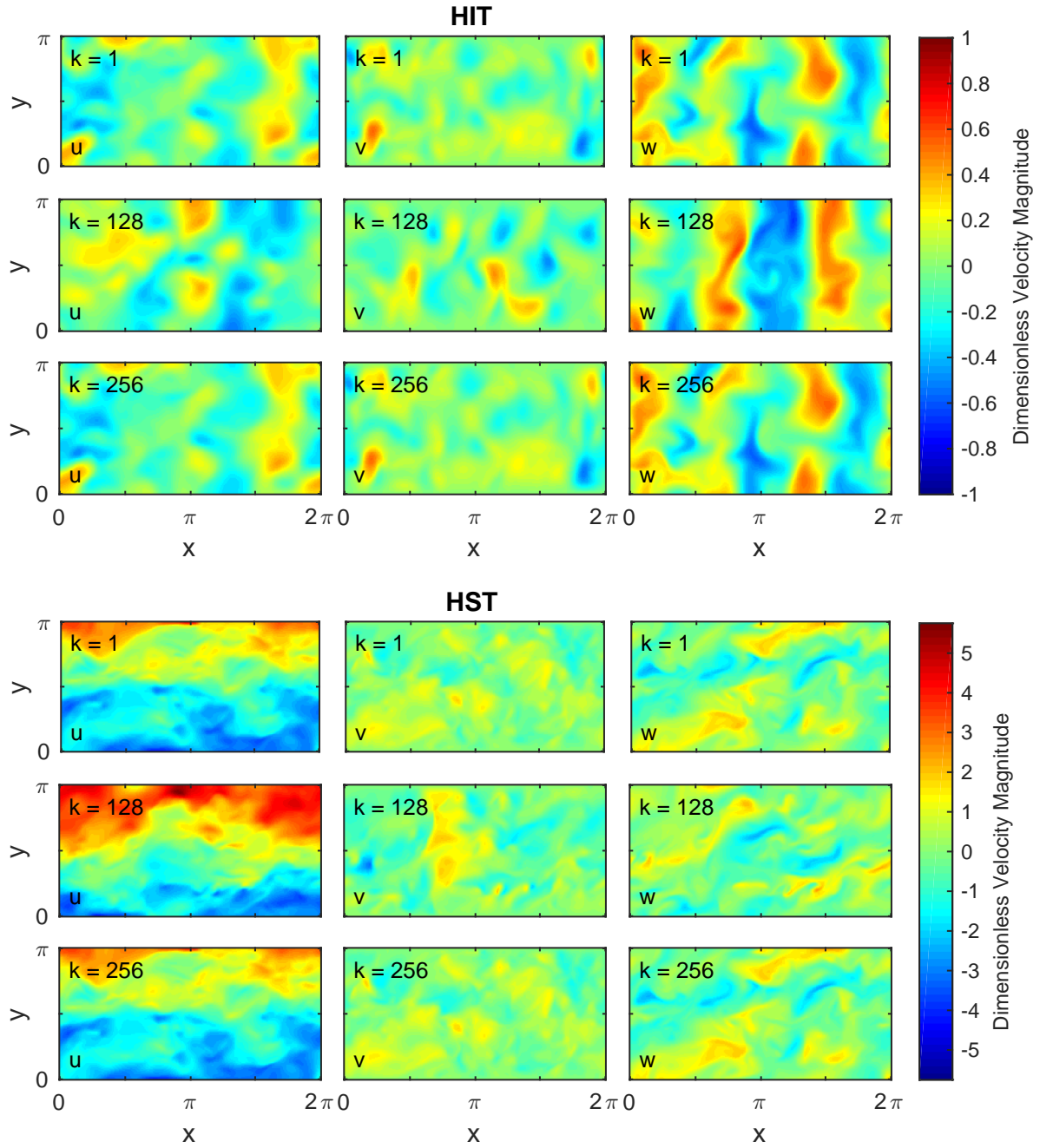
Figure 2: Cartesian velocity components in three slice planes for the isotropic (HIT) and shear (HST) cases. Note that color scales are not identical between cases.

Problem 1.5

We now calculate the xz-averages of all three velocity components for each turbulence case. That is, taking $u_i = \{u, v, w\}$, we calculate

$$\langle u_i \rangle_{xz} (y) = \frac{1}{XZ} \int_{z_{\min}}^{z_{\max}} \int_{x_{\min}}^{x_{\max}} u_i(x, y, z) dx dz. \tag{1}$$
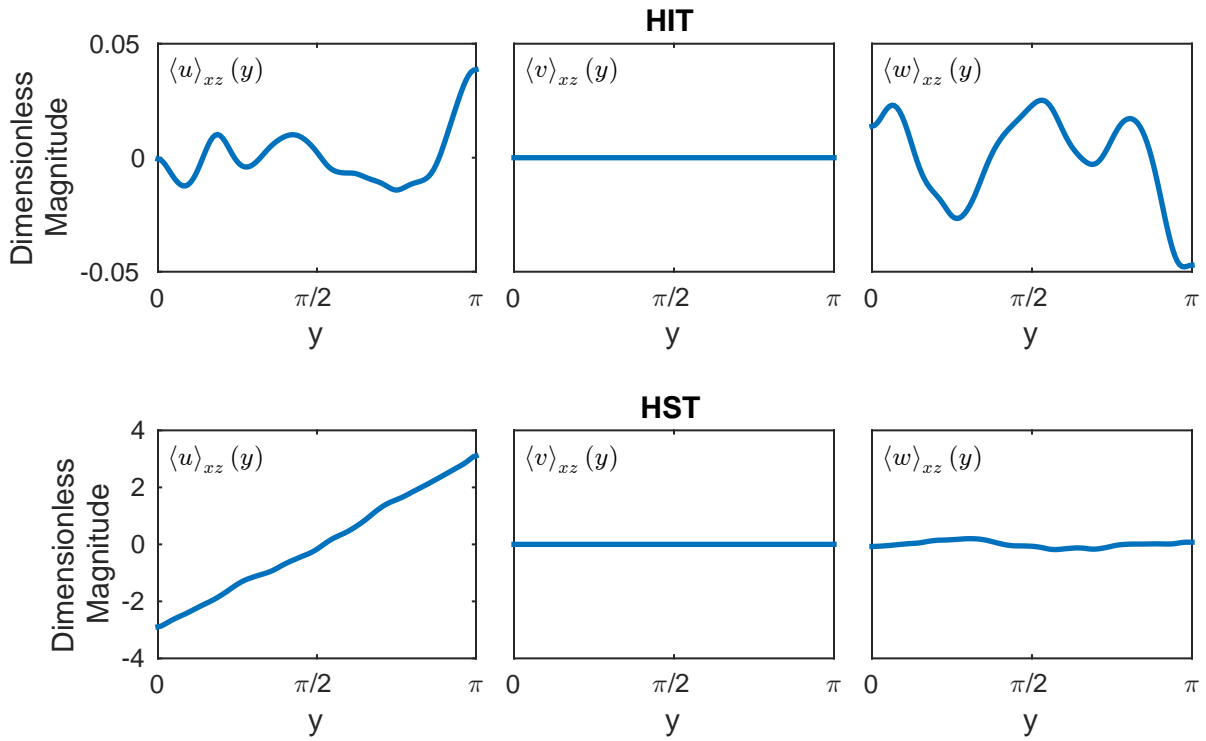
Figure 3: Velocity xz-averages as a function of y-position for the isotropic (HIT) and shear (HST) turbulence cases. Note the disparate scaling between cases.

We wish to apply the definition to our discrete dataset. In discrete form, the integral becomes

$$\langle u_i \rangle_{xz}(y) \rightarrow \frac{1}{N_x N_z} \sum_{k=1}^{N_z} \sum_{i=1}^{N_x} u_i(i, j, k). \tag{2}$$

Carrying out this calculation, we obtain the results shown in Figure 3. The isotropic (HIT) case has near-zero xz-average velocity in all Cartesian directions for all y, though some minor fluctuations are observed in the u- and w-velocities. The shear (HST) case averages show u varying linearly from -3 to 3 as a function of y, whereas the other two components have zero average velocity, independent of y. Both observations confirm our expectations from Problem 1.4 regarding homogeneous directions.

Problem 1.6

We now subtract the xz-average velocities from the slice plane velocity components of Problem 1.3. The results of this calculation for the shear (HST) case,

$$u_i' = u(x, y, z) - \langle u_i \rangle_{xz}(y), \tag{3}$$

are shown in Figure 4. Comparing this to Figure 2, we see that u_i and u_i' are nearly identical for all but the u-velocities. This is to be expected, since $\langle u_i \rangle_{xz}(y) \approx 0$ for all but $i = 1$. In this unique case, we see periodic boundary conditions again emerge between the $y = 0$ and $y = \pi$ bounding planes with respect to velocity *fluctuation*. We also see that $\langle u' \rangle = 0.63$ is positive in the midplane located at $k = 128$, but that $\langle u' \rangle = -0.50$ is negative at the bounding planes, though this disparity could very well be transient.
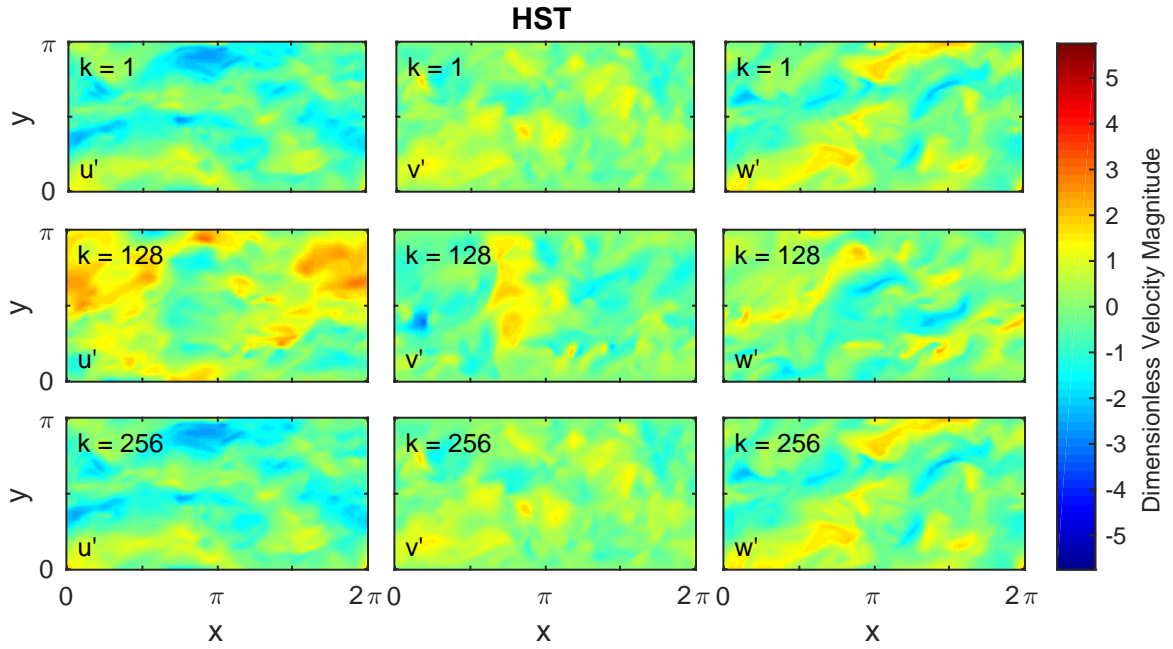
Figure 4: Cartesian velocity fluctuation components $u'_i = u_i - \langle u_i \rangle_{xz}(y)$ in three slice planes for the shear (HST) case. Compare to Figure 2, which uses the same colorbar scale.
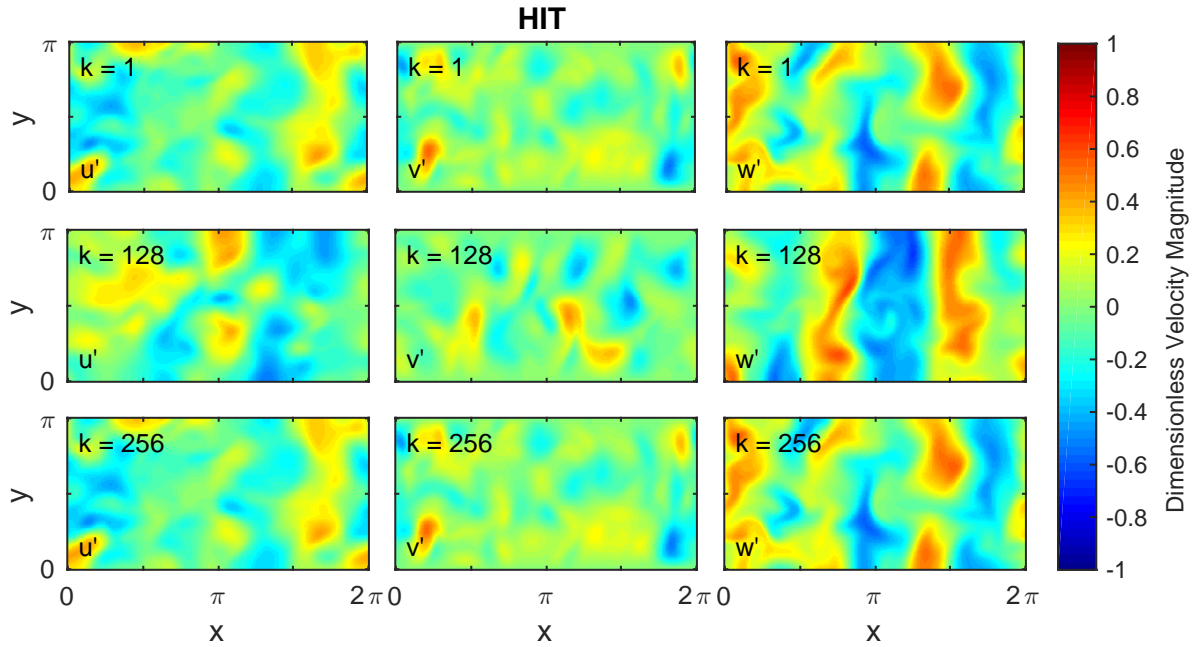

Figure 5: Cartesian velocity fluctuation components $u'_i = u_i - \langle u_i \rangle_{xyz}$ in three slice planes for the isotropic (HIT) case. Compare to Figure 2, which uses the same colorbar scale.
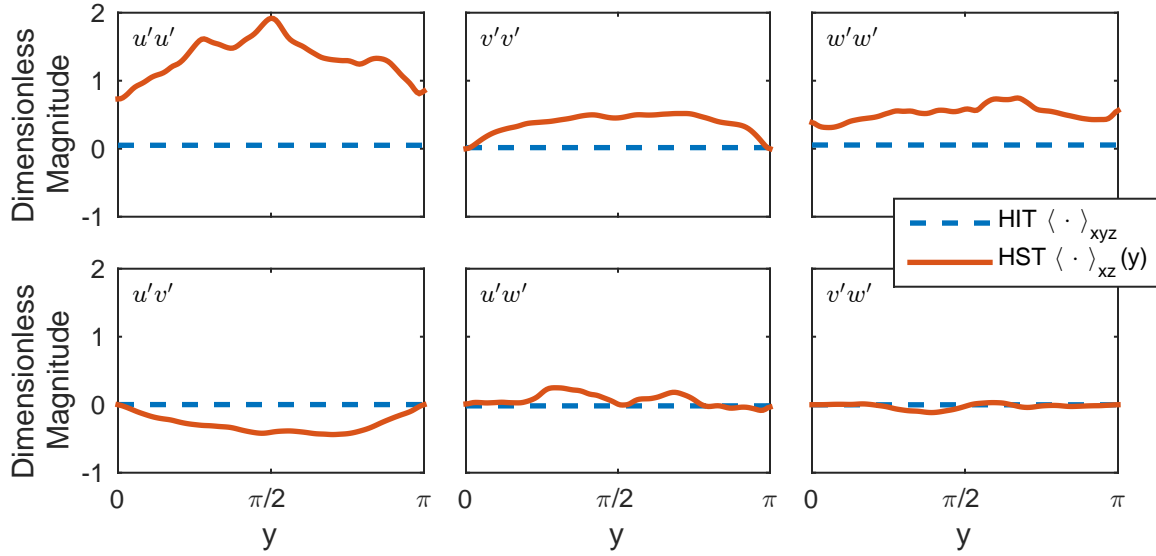
Figure 6: Independent Reynolds stresses for the isotropic (HIT) and shear (HST) cases. Note the HIT stresses have been averaged over the entire domain, whereas the HST stresses retain their y-dependence.

Problem 1.7

Next, we subtract the xyz-average velocities from the slice plane velocity components of Problem 1.3. The results of this calculation for the isotropic (HIT) case,

$$u_i' = u(x, y, z) - \langle u_i \rangle_{xyz}, \tag{4}$$

are shown in Figure 5. Comparing this to Figure 2, we see that u_i and u_i' are nearly identical for all i. This is expected, as $\langle u_i \rangle_{xyz}$ is negligible compared to typical velocity magnitudes of the isotrpic case.

Problem 1.8

Reynolds stresses play an important role in transport equations, and we turn to them now. For the shear (HST) case, we calculate $\langle u_i' u_j' \rangle_{xz}(y)$ to account for the anisotropic y-direction. In Figure 6, this is compared to the single-valued Reynolds stresses $\langle u_i' u_j' \rangle_{xyz}$ of the isotropic (HIT) case, represented as horizontal lines for each combination of i and j. Some Reynolds stresses are redundant due to the commutative property of multiplication, and thus only the six independent Reynolds stresses are shown.

All isotropic (HIT) Reynolds stresses are effectively zero, whereas non-zero values are almost entirely absent from the shear (HST) flow. Since Reynolds stresses act as production terms in the Reynolds-decomposed vorticity transport equation, it is unsurprising that such stresses manifest in a shear flow. The greatest shear stresses are $\langle u'u' \rangle_{xy}$ in the HST flow, corresponding to velocity fluctuations in the direction of applied shear.

Problem 1.9

For the fluctuating velocity $u' = u - \langle u \rangle$, we now calculate the $n = \{2, 3, 4\}$ moments for the HIT and HST data using the appropriately defined averages $\langle u \rangle$ in each case. Skewness and kurtosis values are obtained from these moments, and are plotted for each case in Figure 7.
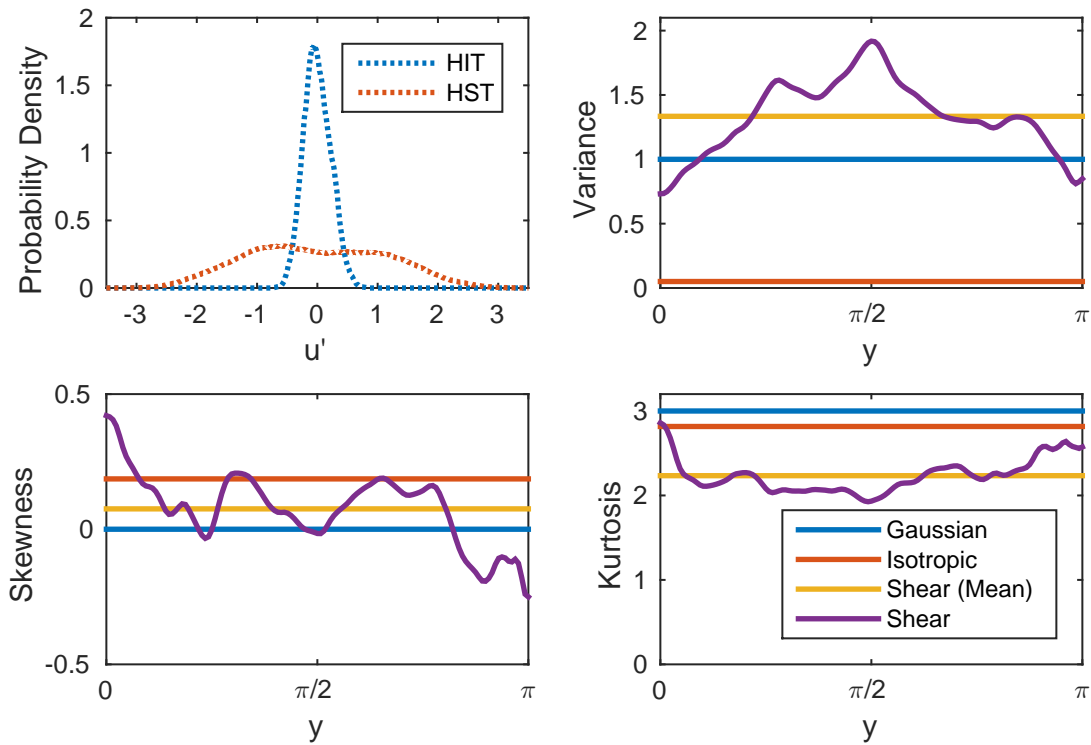
Figure 7: Variance, skewness, and kurtosis of the isotropic (HIT) and shear (HST) fluctuation velocities. PDFs over the entire domain for both cases are included for qualitative reference, as are moments of an ideal Gaussian distribution. Shear moments are plotted as a function of y since they are calculated using the PDF of $u'(y) = u - \langle u \rangle_{xz}(y)$. Isotropic moments use $u' = u - \langle u \rangle_{xyz}$, and are thus single-valued. For data processing, 1200 uniform bins over the interval $u' \in [-6, 6]$ are used. However, the PDFs shown have been made independent of bin size, and reflect the continuous nature of the fluctuation velocities.

Comparing the skewness and kurtosis of u' for the two cases, it is apparent that neither matches a Gaussian distribution exactly. Both isotropic and shear turbulence exhibit higher skewness and lower kurtosis than a process governed by ideal Gaussian statistics. The presence of mean shear brings the skewness closer to that of Gaussian statistics compared to an isotropic flow. However, whereas the kurtosis of isotropic turbulence is within a few percent of the Gaussian value, mean shear significantly decreases the kurtosis.

Problem 1.10

Figure 8 shows the probability density functions of u', v', and w' in the full volume for the isotropic (HIT) case, and in each of the three xz-planes at $j = \{32, 64, 96\}$ for the shear (HST) case. Gaussian distributions using the same mean and variance as each set of data are included for comparison.

From this plot, we can see that the PDFs of u', v', and w' vary little qualitatively between different values of j. Note that the difference in 'roughness' between HIT and HST plots is a direct consequence of different sample sizes filling a constant number of bins. The isotropic PDFs appear similar to the shear PDFs, but the isotropic ones are better approximated by a Gaussian distribution, at least in the x- and z-directions. Both exhibit non-Gaussianity though: HIT has a far sharper peak at the center of the
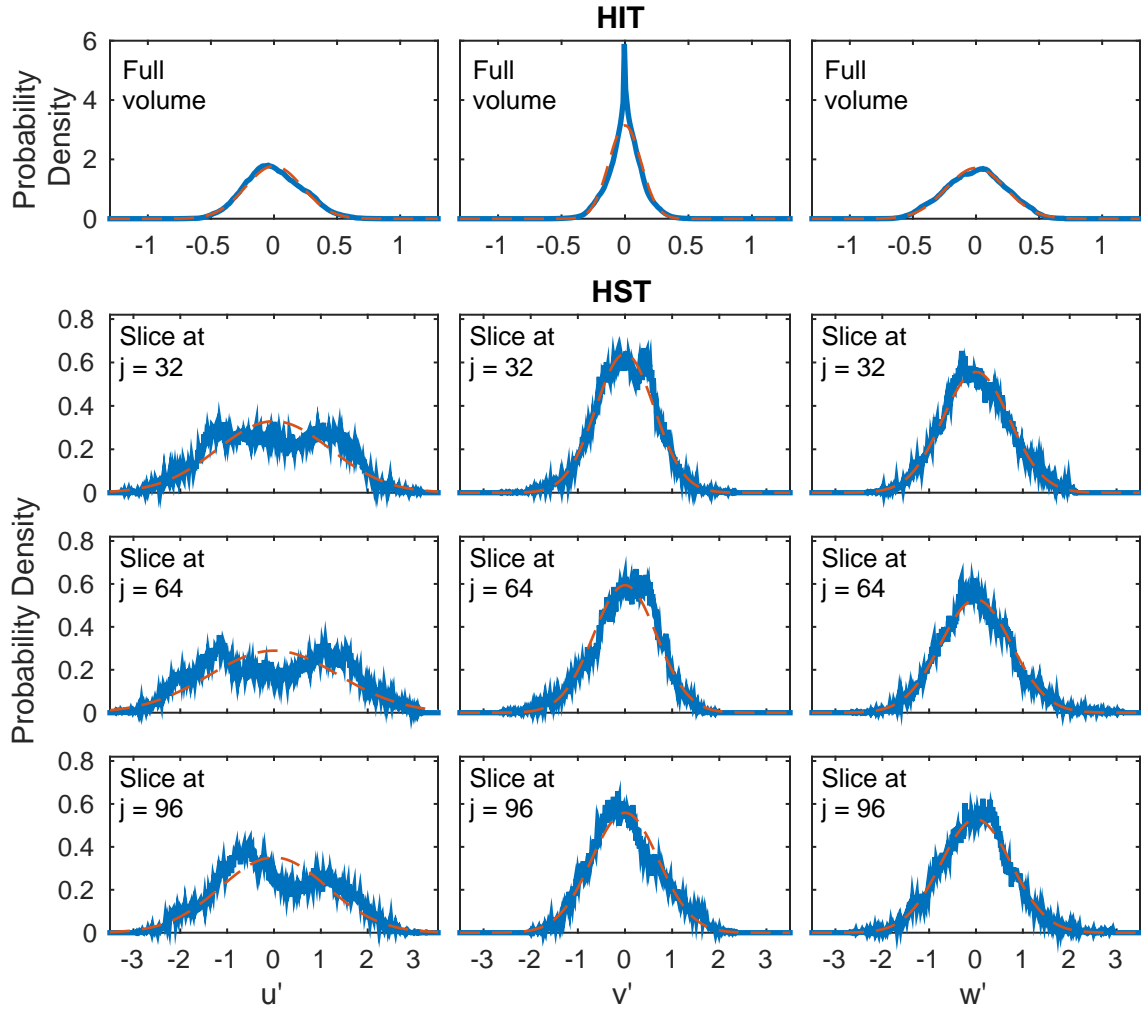
Figure 8: PDFs of fluctuation velocities (━━). Corresponding Gaussian distributions (• • •) parameterized by identical first and second moments are included for comparison. HIT statistics are calculated over the full domain, whereas HST statistics are shown in three different slice planes at $j = \{32, 64, 96\}$.

v' distribution than a Gaussian would, and HST velocity fluctuations in the direction of applied shear (u') are highly bimodal. Note that the velocity magnitudes of the HST case, as has been previously discussed, have a wider range than the HIT case by about $6\times$.

These plots confirm that turbulent statistics are highly non-Gaussian, even in the isotropic case. The presence of mean shear increases the departure from Gaussian statistics, as evinced by the bimodal nature of the u' PDFs. This *suggests a disruption of the energy cascade* in flows with mean shear. That is, the preferential distribution of fluctuation velocities about two concentrations of equal non-zero magnitude suggests that they are "bunching up" there, and have a harder time transfering kinetic energy to smaller length-time scales.

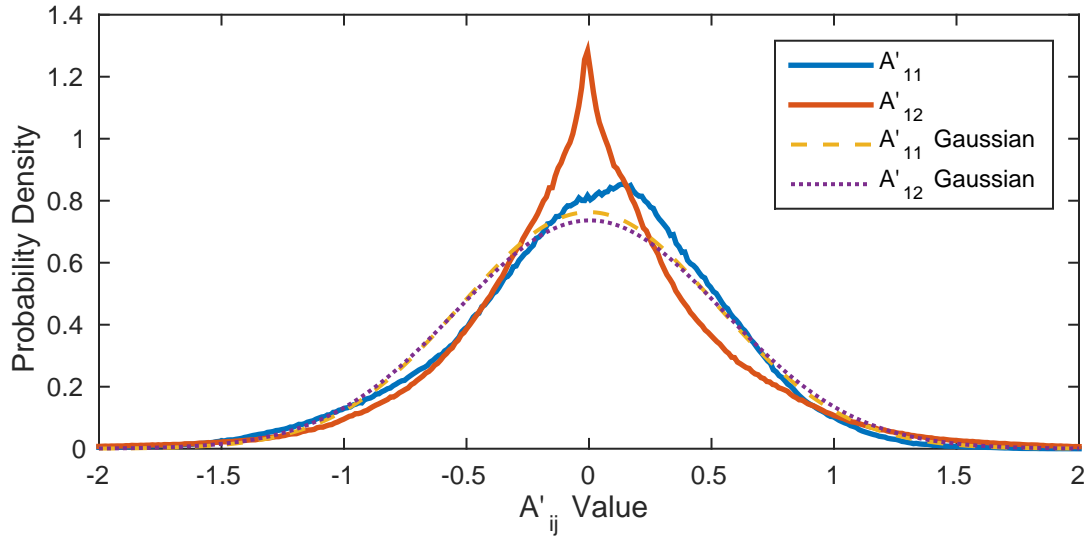## Part 2   Analysis of Velocity Gradients in HIT

Figure 9: PDFs of the fluctuating velocity gradients A'_{11} and A'_{12} over the entire domain. Gaussian fits plotted for comparison.

Problem 2.1

The volume average of the velocity gradient tensor is

$$\langle A_{ij} \rangle_{xyz} = \begin{bmatrix} 2.7474 \times 10^{-08} & 1.2382 \times 10^{-02} & 7.3195 \times 10^{-06} \\ 5.1524 \times 10^{-06} & -3.1956 \times 10^{-11} & 1.0050 \times 10^{-06} \\ -1.0693 \times 10^{-05} & -1.9175 \times 10^{-02} & -1.4207 \times 10^{-08} \end{bmatrix}.$$

For ideal HIT, we would expect to see

$$\langle A_{11} \rangle = \langle A_{22} \rangle = \langle A_{33} \rangle, \tag{5}$$

and that

$$\langle A_{12} \rangle = \langle A_{13} \rangle = \langle A_{21} \rangle = \langle A_{23} \rangle = \langle A_{31} \rangle = \langle A_{32} \rangle. \tag{6}$$

This relationship is roughly borne out by the data. Our diagonal values are very small compared to the mean velocity magnitudes we see in the HIT data, and are thus essentially zero. Magnitudes are similarly small on the off-diagonal, but it is difficult to say that relation (6) is entirely satisfied. As a whole, taking into acount the small magnitudes, the data appears to be reasonably isotropic.

Problem 2.2

Figure 9 shows PDFs of A'_{11} and A'_{12}, and compares them to Gaussian distributions with matching first and second moments. It is clear that the fluctuating velocity gradients are highly non-gaussian, especially A'_{11}. This is to be expected, since the statistics of a turbulent flow quantity become increasingly less Gaussian when we take their derivatives. As a case in point, note that the PDF of u' in Figure 8 was rather well approximated by a Gaussian. The spatial derivatives of u' shown here—in directions parallel and perpendicular to the velocity—are distinctly non-Gaussian however.
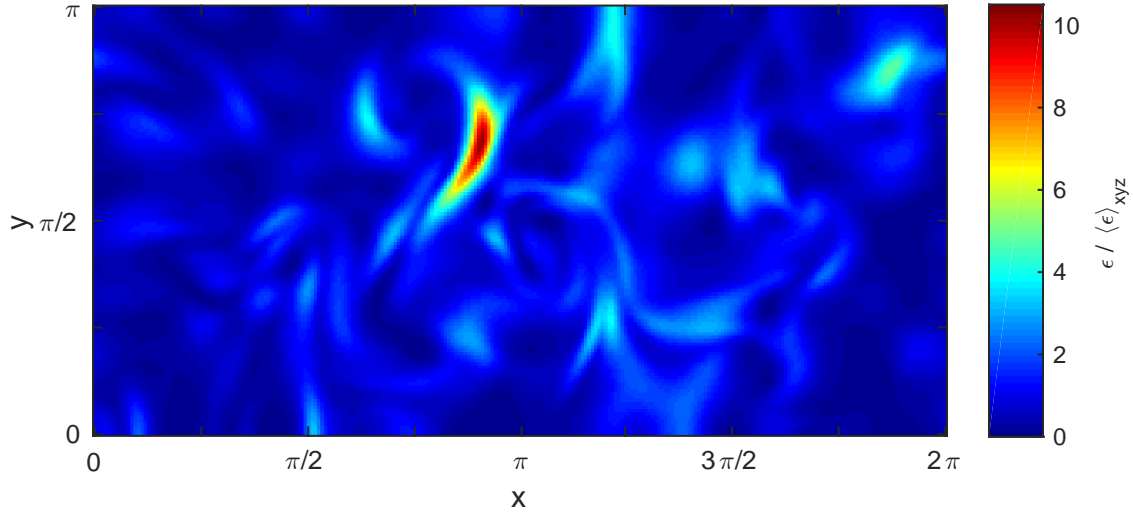
Figure 10: Slice of the normalized pseudo energy dissipation rate field $\epsilon / \langle \epsilon \rangle_{xyz}$ at $k = 128$.

Problem 2.3

The skewness of A'_{11} is -0.320, and the kurtosis of A'_{11} is 3.56. Gaussian distributions have a skewness of 0 and a kurtosis of 3. This tells us that the statistics of velocity gradients in turbulent flows are more sharply peaked and can tend to favor a positive or negative velocity compared to Gaussian statistics.

Problem 2.4

The fluctuating strain rate field $S'_{ij}(x, y, z)$ is given by

$$S'_{ij}(x, y, z) = \frac{1}{2} \left[A'_{ij}(x, y, z) + A'_{ji}(x, y, z) \right], \tag{7}$$

which is just the symmetric part of A'_{ij}.

This quantity can be used to calculate the pseudo energy dissipation rate,

$$\epsilon / \nu \equiv 2 S'_{ij} S'_{ij}. \tag{8}$$

Applying this calculation to our HIT data set, we find the volume average of the pseudo energy dissipation rate to be

$$\boxed{\frac{\langle \epsilon \rangle_{xyz}}{\nu} = 2.85}.$$

Problem 2.5

Figure 10 shows a two-dimensional slice of the normalized pseudo energy dissipation rate field $\langle \epsilon \rangle / \langle \epsilon \rangle_{xyz}$ at $k = 128$. If we compare this to the u'_i velocity fields at $k = 128$ in Figure 5, it is apparent that the local dissipation maxima are located in regions characterized by steep velocity gradients. For example, the dissipation maximum in Figure 10 can be attributed to the w'-velocity gradient in the x-direction located near $x = \pi$ and $y = 2\pi/3$. This makes physical sense, because regions of high shear dissipate energy—the Burgers equation is a perfect example of this.

Problem 2.6

We next calculate the fluctuating vorticity field

$$\omega_i'(x, y, z) = \epsilon_{ijk} A_{kj}', \tag{9}$$

and subsequently the enstrophy field,

$$\Omega(x, y, z) \equiv \frac{1}{2} \omega_i' \omega_i'. \tag{10}$$

For our HIT data set, we find the average value of the enstrophy field to be

$$\boxed{\langle \Omega \rangle_{xyz} = 1.42}.$$

Problem 2.7

Writing out the expressions for ϵ/ν and Ω in terms of A_{ij}', and subsequently averaging over space and employing relations (5) and (6), as well as the moment relations in Section 6.2 of *Dahm and Hamlington*, it is possible to arrive at the analytical expressions

$$\frac{\langle \epsilon \rangle_{xyz}}{\nu} = 6 \left[\overline{A_{11}^2} + \overline{A_{12}^2} + \overline{A_{12} A_{21}} \right] \tag{11}$$

$$\langle \Omega \rangle_{xyz} = 3 \left[\overline{A_{12}^2} - \overline{A_{12} A_{21}} \right]. \tag{12}$$

Combining these expressions yields the relationship

$$\frac{\langle \epsilon \rangle_{xyz}}{\nu} = 6 \left[\overline{A_{11}^2} + \frac{\langle \Omega \rangle_{xyz}}{3} + 2\overline{A_{12} A_{21}} \right] \tag{13}$$

We now analyze each of these terms within the data set. For the first term, $\overline{A_{\alpha\alpha}^2}$, where no summation is implied over greek letters by convention, we calculate

$$\overline{A_{11}^2} = 0.273,$$
$$\overline{A_{22}^2} = 0.160,$$
$$\overline{A_{33}^2} = 0.272, \qquad \text{with an average of } 0.235. \tag{14}$$

For the third term, we calculate $2\overline{A_{\alpha\beta} A_{\beta\alpha}}$, where $\alpha \neq \beta$. Our results are

$$2\overline{A_{12} A_{21}} = -0.160,$$
$$2\overline{A_{13} A_{31}} = -0.385,$$
$$2\overline{A_{23} A_{32}} = -0.156, \qquad \text{with an average of } -0.234. \tag{15}$$

Thus, the first and third terms on the right-hand side of (13) cancel out when we take full averages *in our data set*. I have not been able to provide a compelling reason why this occurs, although it should be noted that our calculations in (14) and (15) show that the turbulence is not very isotropic since the equivalence of second-order moments does not hold. We could hypothesize that the terms in question will always be of opposite sign and similar magnitude, but I would like to know the explicit reason if one exists.

In any case, taking a full average of our data causes these terms to cancel, and (13) becomes

$$\langle \epsilon \rangle_{xyz} \approx 2 \langle \Omega \rangle_{xyz}, \tag{16}$$

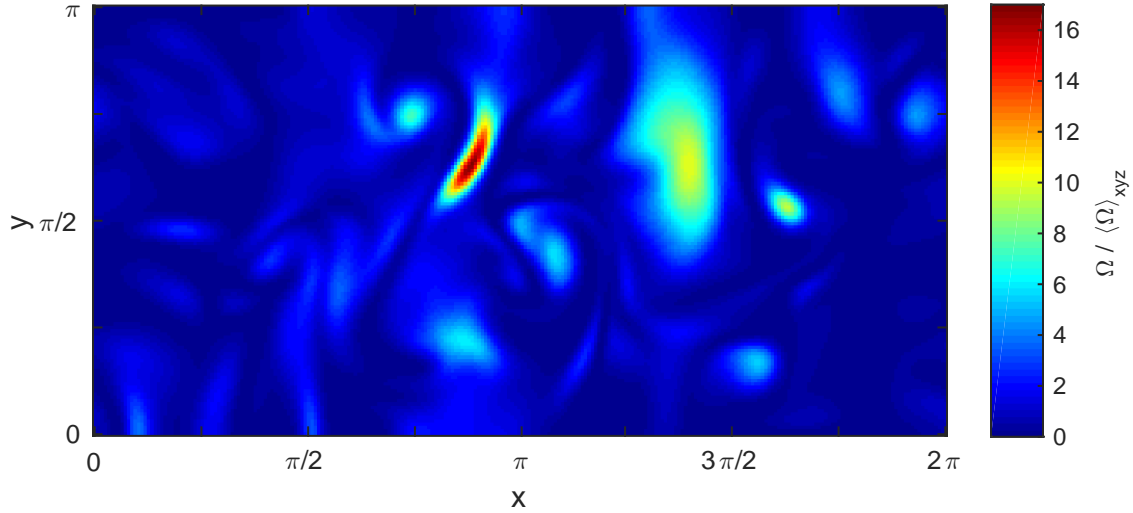which is borne out in our data, since $2.85 \approx 2 \times 1.42$.

Figure 11: Slice of the normalized enstrophy field $\Omega/\left\langle\Omega\right\rangle_{xyz}$ at $k = 128$.

Problem 2.8

A slice of the normalized enstrophy field at $k = 128$ is presented in Figure 11. We can draw comparisons between this field and our u'_i field (Figure 5) and normalized dissipation field (Figure 10).

   First of all, enstrophy is vorticity magnitude, and thus the enstrophy field highlights cores of vortical structures in the flow. These vortical structures can be seen in the u'_i slices, and are clearly picked up by our enstrophy slice. Furthermore, most energy dissipation occurs some small radius away from the centers of these structures, as can be seen by comparing the enstrophy and dissipation fields. Of course, a transient shear layer will have high vorticity and also high dissipation, which explains the spatial coincidence of the maxima in Figure 10 and Figure 11.

Problem 2.9

Probability density functions of $\epsilon/\left\langle\epsilon\right\rangle_{xyz}$ and $\Omega/\left\langle\Omega\right\rangle_{xyz}$ are displayed in Figure 12. Both appear to approximate log-normal statistics, which is expected since they are multiplicative quantities.

   The normalized enstrophy field, which again corresponds to vorticity magnitude, is skewed heavily toward zero. We attribute this to the fact that vorticity is highly localized. Due to the Biot-Savart law, vorticity magnitudes are very small over most of the fluid domain since induced vorticities tend to cancel out away from vortex cores. This strong spatial concentration of enstrophy can be seen in Figure 11.

   The normalized energy dissipation rate field has a more relaxed PDF, owing to the fact that energy dissipation is spread somewhat more evenly throughout the flow. Shear is a less localized quantity than vorticity magnitude, as can be seen in 10.
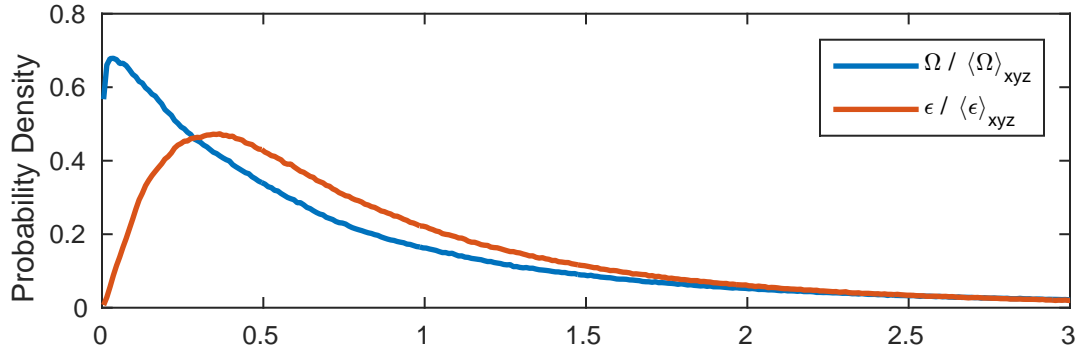
Part 3   Advanced Topics

Figure 12: PDFs of the normalized pseudo energy dissipation field $\epsilon/\langle\epsilon\rangle_{xyz}$ and the normalized enstrophy field $\Omega/\langle\Omega\rangle_{xyz}$ over the full fluid domain.

Problem 3.1

For the HIT case, we calculate the u-velocity autocorrelation function $\rho(r)$, defined as

$$\rho(r) \equiv \frac{\langle u'(x,y,z)u'(x+r,y,z)\rangle_{xyz}}{\langle u'^2\rangle_{xyz}}, \tag{17}$$

taking periodic boundary conditions into account. Our results are presented over the domain $r \in [0, \pi]$, since $r = \pi$ is the farthest away from a point we can go in a 2π-periodic domain before approaching at a radius $r < \pi$ from the opposite side.

Our autocorrelation function is shown in Figure 13. From $\rho(r)$, we can calculate the corresponding spatial integral scale

$$\Lambda \equiv \int_0^\infty \rho(r)dr \approx \int_0^\pi \rho(r)dr = 0.458, \tag{18}$$

and the spatial Taylor scale λ, where

$$\lambda^2 \equiv -2\left(\left.\frac{d^2p}{dr^2}\right|_{r=0}\right)^{-1} \approx 0.606. \tag{19}$$

For the integral scale, we set the upper bound of the integral to π, since it is the largest possible radius in this periodic domain, as discussed above. It is difficult to define a true integral scale for this dataset. For the Taylor scale, we approximate the derivative using a fourth-order one-sided difference formula.

In addition to the autocorrelation and the two spatial scales, a Gaussian and an exponential fit to $\rho(r)$ are plotted in Figure 13. These fits are parameterized by the integral scale as

$$\text{exponential} = \exp\left[\frac{r}{\Lambda}\right], \qquad \text{Gaussian} = \exp\left[-\frac{\pi}{4}\left(\frac{r}{\Lambda}\right)^2\right].$$

Because $\rho(r)$ is approximated much better by the Gaussian and the exponential, our Reynolds number must be fairly small.

Problem 3.2

The joint PDF of $\epsilon/\langle\epsilon\rangle_{xyz}$ and $\Omega/\langle\Omega\rangle_{xyz}$, normalized by the marginal product of their individual PDFs is presented in Figure 14. In short, we plot the quantity $I(\epsilon/\langle\epsilon\rangle_{xyz}, \Omega/\langle\Omega\rangle_{xyz})$, where

$$I(a,b) = \frac{\beta(a,b)}{\beta(a)\beta(b)}, \tag{20}$$

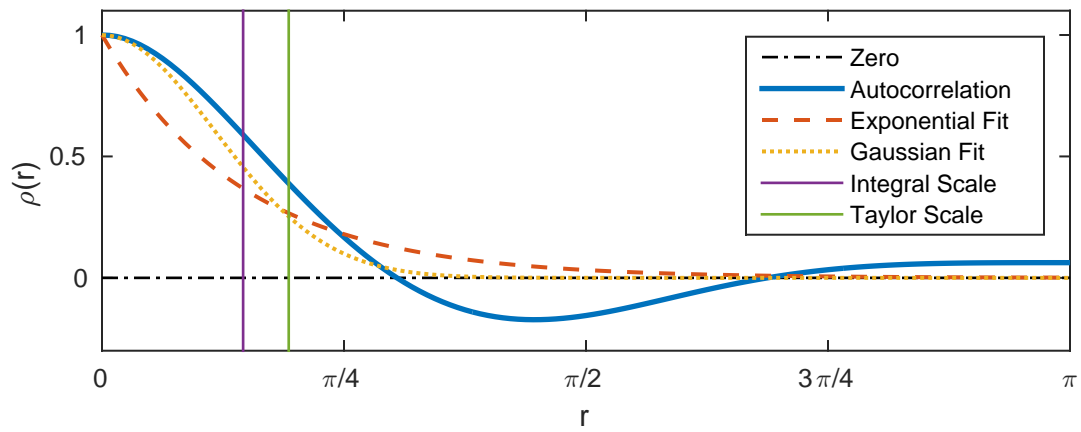**Figure 13:** Blep.

and β denotes a probability density function. This figure tells us that spatially, large values of ϵ tend to correspond to large values of Ω, and vice versa.
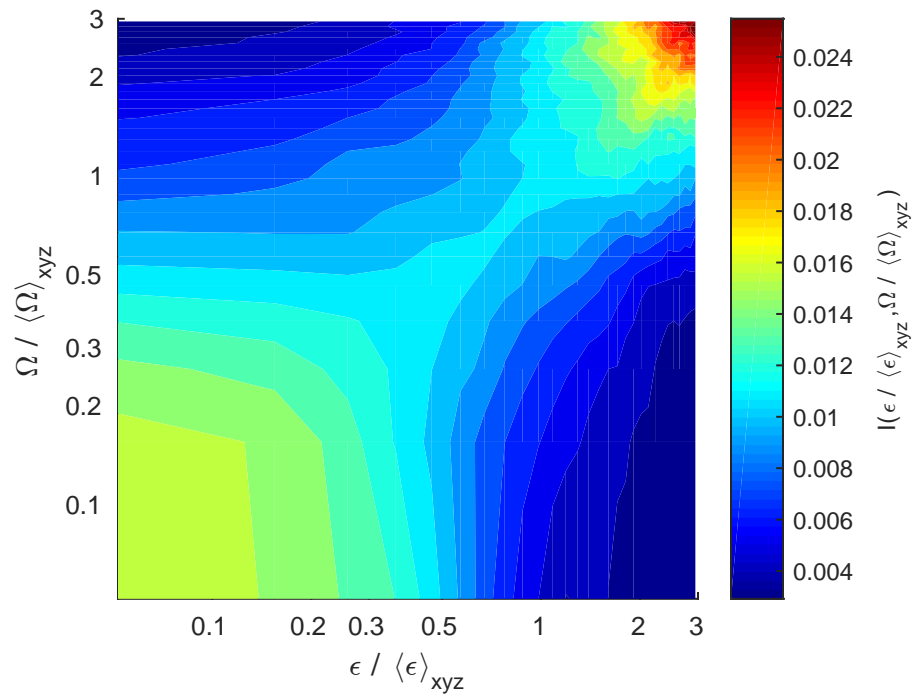
Figure 14: Joint PDF of $\epsilon/\langle\epsilon\rangle_{xyz}$ and $\Omega/\langle\Omega\rangle_{xyz}$, normalized by the marginal product of both individual PDFs. Log axes are used since the component quantities approximate log-normal statistics.